Galindo, J.; Serrano Cruz, JR.; Piqueras, P.; Garcia Afonso, O. (2012). Heat transfer modelling in honeycomb wall-flow diesel particulate filters. Energy. 43:201-213. doi:10.1016/j.energy.2012.04.044.

Heat transfer modelling in honeycomb wall-flow diesel particulate filters

José Galindo, José Ramón Serrano, Pedro Piqueras *, Óscar García-Afonso

Universitat Politècnica de València, CMT-Motores Térmicos, Camino de Vera s/n, 46022 Valencia, Spain.

Abstract

Heat transfer in wall-flow monoliths has gained in interest because of the widespread adoption of these systems by automotive industry to fulfil soot emission regulations and the importance of heat exchange on the regeneration process control to avoid damaging the monolith. This paper presents a heat transfer model for wall-flow diesel particulate filters coupled with an unsteady compressible flow solver. The heat exchange between the gas and the solid phase is based on a bi-dimensional discretisation of the porous medium both in axial and tangential directions. The monolith can be discretised in the radial direction to account for the heat fluxes towards the environment through the monolith and the canister, which is also coupled with the inlet and outlet ducts of the filter. The model is validated against experimental data obtained in a flow test rig. A test campaign under non-reacting conditions has been conducted to show the capability for thermal response prediction. Tests cover clean and soot loaded monolith, continuous flow under steady and transient thermal conditions, and pulsating flow. In this case, the characteristics of the pressure waves in amplitude and frequency are similar to those that the monolith can undergo depending on its location along the exhaust line.

Keywords: Diesel engines, aftertreatment, diesel particulate filter, heat transfer, modelling, experiments

1. Introduction

The fulfilment of current and future soot emissions regulations in Diesel engines have led to the widespread use of diesel particulate filters (DPFs). These systems were identified more than thirty years ago as the most effective system to control aerosol emissions in Diesel engines. However, commercial applications have been delayed up to ten years ago [1] because of the interaction of several interdisciplinary aspects. On the one hand, the inclusion of a specific soot aftertreatment system involves itself the increase of the engine cost. As a consequence, DPFs use was displaced for the time in which soot emission limits imposed by pollutants regulations were fulfilled by means of other improvements in the engine [2] regarding the injection [3] and the combustion processes and technology [4, 5], the control of Diesel engines transient behaviour [6, 7] and the understanding of pollutants formation during these phases [8, 9], flexible turbocharging systems [10] or exhaust gas recirculation [11].

*P. Piqueras. CMT-Motores Térmicos, Universitat Politècnica de València, Camino de Vera s/n, 46022 Valencia, Spain.
Phone: +34 963877650 Fax: +34 963877659 e-mail: pedpicab@mot.upv.es

The damage to specific fuel consumption caused by increasing exhaust line back-pressure as the DPF becomes loaded [12] requires the regeneration of the DPF. The early use of DPFs would have meant to deal with important problems regarding safe reliable regeneration under all driving conditions. The need of periodic controlled regeneration occurrences to drive the system towards low back-pressure were complex and costly. Nowadays, regeneration is still one of the most critical issues regarding DPF operation due to its effects on monolith useful life [13]. Significant efforts have been driven in recent years to the development of regeneration modelling tools [14] in order to characterise regeneration phenomena under a wide spectrum of operating conditions. However, a reliable prediction of the DPF durability is also highly dependent on the heat transfer response of the DPF monolith and canister. The need for DPF designs driving to adiabatic operation [15] may be opposite to mechanical integrity, as forward shown in this work. The trade-off between optimum thermal behaviour of the DPF and its durability is specially outstanding in pre-turbo DPF configurations, in which thermal losses and mechanical loads become more marked independently of the type of engine, i.e. passenger car engines [16], heavy duty engine for transport applications [17] and non-road vehicles [18].

Additionally, high filtration efficiency and low pressure drop performance are expected characteristics for soot filtration systems closely related themselves. They can come linked and often in conflict with regeneration and thermal response. Hence the importance of robust computational tools integrating specific submodels for every physical-chemical process taking place in the DPF [19, 20]. According to this objective, this work presents a heat transfer model for honeycomb wall-flow DPFs comprising gas to solid substrate and subsequent monolith to environment heat exchange.

Heat transfer has been studied in monolith structures for catalytic applications but not in depth for wall-flow monoliths, which show different flow field in inlet and outlet channels. Groppi and Tronconi [21] approached for a continuum calculation of the heat transfer process in non-adiabatic honeycomb monolith structures. In order to account for the effect of heat exchange in the radial direction they provided an expression for the determination of the effective radial conductivity of the monolith. This calculation is based on the analysis of the equivalence thermal resistance scheme in a unit cell. The proposed model was applied to the analysis and design of high conductivity supports in which conduction would prevail over convection as the dominant heat transfer process and contribute to the avoidance of hot spots appearance [22]. In the field of wall-flow DPFs, Haralampous *et al.* investigated the suitability of uniform soot particulate layer temperature assumption in the tangential direction [23]. For this purpose, a one-dimensional model was proposed to solve the heat transfer inside the soot layer and the porous wall along the flow direction through the wall. However, the monolith thermo-and flow dynamics was approximated by means of a zero-dimensional model assuming (i) all channels behave identical, what implies radial heat losses are negligible and uniform radial flow distribution; (ii) uniform soot deposition along the inlet monolith channels; and (iii) equal exhaust gas temperature along the inlet channel length. In more recent works, Haralampous *et al.* focus on chemical aspects regarding regeneration and gas phase reactions applying a one-dimensional quasi-steady model to the flow dynamic simulation inside the monolith channels but assuming negligible radial heat transfer to ambient [24, 25], as commonly

assumed in the literature. Thus, Lee *et al.* [13] account for conductive radial heat transfer but outer wall completely insulated in the analysis of the influence that the monolith geometry has on the thermal response during regeneration; Schejbal *et al.* [26, 27] assume negligible radial heat transfer in its studies regarding regeneration process in soot filter systems.

The present work proposes a heat transfer model for honeycomb wall-flow DPFs. The model is based on a bi-dimensional discretisation of the porous medium (particulate layer and porous substrate) between a pair of inlet and outlet channels accounting for gas to solid heat transfer and heat conduction across the substrate both in the axial and the tangential directions. The model allows the radial discretisation of the monolith into concentric channel beams. All the pairs of inlet and outlet channels contained in every channel beam are assumed to have the same flow properties profile in the axial direction. The radial heat fluxes are modelled by means of equivalent thermal resistances linking adjacent channel beams, so that the model provides the temperature flow field in the radial and axial direction assuming an axisymmetric distribution. Finally, the canister is coupled with the external channel beam and discretised axial-and radially to consider the effect of every one of its layers on the heat exchange with the environment and the elements connected at the inlet and outlet of the DPF. The model is validated against a set of experimental data obtained under non-reacting conditions in a flow test rig. Tests cover clean and loaded monolith, steady flow conditions during steady and transient thermal operation, and pulsating flow of different amplitude and frequency to represent a wide spectrum of in-engine DPF operation.

2. Heat transfer model

The proposed heat transfer model for honeycomb wall-flow DPFs is based on a nodal discretisation of the monolith porous medium and the external canister. The model solves the general heat transfer equation in the axial and tangential directions. Considering as representative case a node inside the porous wall between a pair of inlet and outlet channels, the heat transfer equation yields:

$$\rho c_p \frac{\partial T}{\partial t} = \left(\frac{\partial^2 T}{\partial x^2} + \frac{\partial^2 T}{\partial z^2} \right) k + \dot{q}''_{chr} \tag{1}$$

The wall temperature at time instant $p+1$ and node (m,n) can be obtained with an explicit solution from the wall temperature at time instant p considering centred finite differences:

$$\rho c_p \frac{T^{p+1}_{m,n} - T^{p}_{m,n}}{\Delta t} = k \frac{T^{p}_{m-1,n} - 2T^{p}_{m,n} + T^{p}_{m+1,n}}{(\Delta x)^2} + k \frac{T^{p}_{m,n-1} - 2T^{p}_{m,n} + T^{p}_{m,n+1}}{(\Delta z)^2} + \dot{q}''_{chr} \tag{2}$$

Taking into account that the thermal properties at every node and the heat transfer area may be different (gas to solid heat transfer, boundary condition discretisation [28], wall temperature distribution affecting thermal properties, radial monolith conduction effect, particulate layer thickness, etc.), the wall temperature can be finally calculated as:

$$T_{m,n}^{p+1} = \frac{\Delta t}{C_{m,n}} \left[\sum_{j=-1}^{+1} \frac{T_{m+j,n}^{p} - T_{m,n}^{p}}{R_{m+j,n/m,n}} + \sum_{j=-1}^{+1} \frac{T_{m,n+j}^{p} - T_{m,n}^{p}}{R_{m,n+j/m,n}} + \dot{q}_{chr} \right] + T_{m,n}^{p} \quad (3)$$

In Eq. (3), $C_{m,n}$ represents the thermal capacity in the control volume of node (m, n) and $R_{m',n'/m,n}$ is the equivalent thermal resistance between nodes (m', n') and (m, n). The source term $\dot{q}_{chr}$ accounts for the heat release per unit of time due to chemical reactions.

2.1. Channel wall temperature calculation

From the general solution to the problem given by equation 3, the main hypothesis taken to describe the temperature field inside the DPF monolith are the following:

- The heat transfer model is coupled with a gas dynamic model to solve one-dimensional unsteady compressible non-homentropic flow in wall-flow diesel particulate filters [19], whose governing equations are formulated in Appendix A. In this way, the solution of Eq. (1) is carried out with the same time-step (Δt) which is applied to solve the flow governing equations inside the monolith channels.

- The model is formulated assuming cylindrical monolith with square channels. Equivalent diameter may be considered in the case of more complex geometries as proposed for elliptic cross-sections by Ilikali *et al.* [29]. In this case, the model would be able to predict heat fluxes and therefore outlet gas temperature but not in-monolith temperature field.

- The porous walls are considered plane sheets, so that the general form of the equivalent thermal resistances and the thermal capacity is:

$$R_{conv} = \frac{1}{Fh} \;\; ; \;\; R_{cond} = \frac{l}{Fk} \;\; ; \;\; C = \rho c_p V \quad (4)$$

- The monolith can be discretised in the radial direction by means of concentric channel beams [19], so that radial heat transfer and flow mal-distribution can be computed. The flow properties profile in the axial direction is the same for all the channels in the same beam. Consequently, only one pair of inlet and outlet channels must be solved per channel beam.

- Radial heat transfer is considered between adjacent channel beams.

- The external channel beam is connected by an equivalent thermal resistance to the mat and the metal can of the DPF in order to account for heat transfer to the environment.

- Axial heat conduction in the gas phase and radiation inside monolith channels are assumed negligible.

The thermal equivalent scheme for the channel wall temperature calculation in every axial location is shown in Figure 1. This scheme is centred on node m in channel beam H. The wall axial discretisation fits in with the axial discretisation of the channels for the solution of the flow governing equations.

The porous wall is discretised in every axial location in the tangential direction by means of three nodes, which are placed: the first one on the interface between the inlet channel and the porous wall (or the particulate layer if exists) ($T^H_{m,1}$); the second one in the middle of the porous wall ($T^H_{m,2}$); and the third one on the interface between the porous wall and the outlet channel ($T^H_{m,3}$). This tangential discretisation of the porous medium allows the consideration of temperature gradients between the soot layer and the porous substrate, whose influence was studied by Haralampous and Koltsakis [23]. The model considers the heat transfer due to conduction (substrate) and convection (gas phase) by means of equivalent thermal resistances in the tangential direction of the flow advection. Axial conduction in the substrate is also taken into account in the middle node $(m, 2)$. An equivalent thermal capacity, which is defined by the properties of the substrate, is included in every node to account for the thermal inertia effects during transient periods.

Finally, the model includes the radial heat transfer across the monolith by means of its discretisation into concentric channel beams. The equivalent thermal resistance between adjacent channel beams for a channel beam H can be initially defined in cylindrical coordinates as:

$$R^{H,H-1}_{m,2} = \ln\left(\frac{D^H_{ext}}{D^{H-1}_{int}}\right)\frac{1}{2\pi\Delta x k_r} \tag{5}$$

$$R^{H,H+1}_{m,2} = \ln\left(\frac{D^{H+1}_{ext}}{D^H_{int}}\right)\frac{1}{2\pi\Delta x k_r} \tag{6}$$

Eqs. (5) and (6) represent in cylindrical coordinates the conduction heat transfer across the wall of a duct whose thermal conductivity coincides with that of the monolith in the radial direction (k_r), as represented in Figure 2.

The representation of the actual heat flux in a honeycomb monolith, where the gas flows along the channels, is highly dependent on the radial mesh with this kind of discrete approach. As pointed out by Groppi and Tronconi [21], the radial thermal gradient between close channels is very reduced because of the high heat transfer surface. This surface is defined by the cellular geometry of the monolith channels. However, Eqs. (5) and (6) only account for a discrete heat transfer surface given by the contact surface between channel beams. As the number of channel beams is reduced, the difference between the actual heat transfer surface and that considered by the equivalent thermal resistance defined in cylindrical coordinates increases. As a result, the calculated equivalent thermal resistance becomes lower and lower than the actual one and the heat flux is over-predicted.

Therefore, the definition of the thermal equivalent resistance given by Eqs. (5) and (6) needs to be corrected to prevent the heat flux prediction being affected by the radial discretisation. It is proposed a correction based on the ratio between the heat transfer surface of the channels in the control volume and the contact surface between the channel beams. This approach increases the value of the radial equivalent thermal resistance defined by Eqs. (5) and (6)

being such increase controlled by the number of involved channels (actual process) and the size of the discretisation (idealised process).

The proposed corrector factor is a function of the cell size (α), the cell density (σ) and the difference between the diameters defining the boundaries of the channel beams

$$\frac{S_{ht}^{H,H+1}}{S_{contact}^{H,H+1}} = 2\alpha\sigma\left(D_{ext}^{H+1} - D_{int}^{H}\right), \tag{7}$$

so that the calculation of the corrected equivalent thermal resistance is given by

$$R_{m,2}^{(H,H-1)^*} = \alpha\sigma\left(D_{ext}^{H} - D_{int}^{H-1}\right)\ln\left(\frac{D_{ext}^{H}}{D_{int}^{H-1}}\right)\frac{1}{\pi\Delta x k_r}; \tag{8}$$

$$R_{m,2}^{(H,H+1)^*} = \alpha\sigma\left(D_{ext}^{H+1} - D_{int}^{H}\right)\ln\left(\frac{D_{ext}^{H+1}}{D_{int}^{H}}\right)\frac{1}{\pi\Delta x k_r}. \tag{9}$$

The smallest radial discretisation allowed by the monolith is defined by its cellular geometry, i.e. the channel beams have the dimension $\alpha + w_w$ as minimum thickness. Therefore, the limit of the proposed corrector factor is a function of the cellular geometry:

$$\lim_{D_{ext}^{H+1} - D_{int}^{H} \to 2(\alpha + w_w)} 2\alpha\sigma\left(D_{ext}^{H+1} - D_{int}^{H}\right) = \frac{4\alpha}{\alpha + w_w} \tag{10}$$

Figure 3 shows the value of the corrector factor as a function of the normalised number of channel beams in which the monolith cross section is discretised. It is calculated as the ratio between the number of channel beams and the maximum possible number of them, which is defined as the monolith diameter divided into $\alpha + w_w$. The calculation has been performed for two cell densities (200 cpsi and 300 cpsi) varying the channel cell size ±10% with respect to the nominal value (1.486 mm and 1.156 mm respectively). The channel beams have been uniformly distributed, i.e. all of them have the same thickness.

The value of the corrector factor diminishes as the number of channel beams increases. When the maximum refinement of the radial mesh is reached, the corrector factor converges to the value given by Eq. (10), whose order of magnitude is 3.3.

Applying the nodal scheme for the porous substrate, the wall temperature in every node is obtained according to:

$$T_{m,1}^{H^{p+1}} = \frac{\Delta t}{C_{m,1}^{H}}\left[\frac{T_i^{H^p} - T_{m,1}^{H^p}}{R_i^H} + \frac{T_{m,2}^{H^p} - T_{m,1}^{H^p}}{R_{m,1/m,2}^{H}} + \dot{q}_{chr}\right] + T_{m,1}^{H^p} \tag{11}$$

$$T_{m,2}^{H^{p+1}} = \frac{\Delta t}{C_{m,2}^{H}}\left[\sum_{k=1}^{3}\frac{T_{m,k}^{H^p} - T_{m,2}^{H^p}}{R_{m,k/m,2}^{H}} + \sum_{j=-1}^{1}\frac{T_{m+j,2}^{H^p} - T_{m,2}^{H^p}}{R_{m+j,2/m,2}^{H}} + \sum_{h=-1}^{1}\frac{T_{m,2}^{(H+h)^p} - T_{m,2}^{H^p}}{R_{m,2}^{(H,H+h)^*}}\right] + T_{m,2}^{H^p} \tag{12}$$

$$T_{m,3}^{H^{p+1}} = \frac{\Delta t}{C_{m,3}^{H}}\left[\frac{T_{m,2}^{H^p} - T_{m,3}^{H^p}}{R_{m,3/m,2}^{H}} + \frac{T_{o}^{H^p} - T_{m,3}^{H^p}}{R_{o}^{H}}\right] + T_{m,3}^{H^p} \tag{13}$$

$T_i^{H^p}$ and $T_o^{H^p}$ represent the gas temperature in the inlet and outlet channels of beam H at the time instant p respectively. The heat release due to exothermic regeneration reactions ($\dot{q}_{chr}$) is taken into account in the node $(m, 1)$ on the interface between the inlet gas and the porous medium (Eq. 11). Index k takes the values 1 or 3 according to the radial nodes nomenclature, whereas index j is applied to axial nodes being its value -1 or 1. The radial heat transfer is considered with the previous and next channel beams (index h equal to -1 and 1 respectively). In the case of the peripheral channel beam, the radial conduction is considered with the adjacent previous channel beam and with the canister.

2.2. Canister wall temperature calculation

The DPF canister is designed to reduce the thermal losses to the environment, so that a suitable prediction of the gas temperature distribution inside the monolith is dependent on a proper calculation of the surface temperature. The DPF canister is composed of a mat and a metal can surrounding the monolith. Additionally, the model considers the existence of an air gap between the mat and the metal can.

The nodal scheme shown in Figure 4 is proposed to model the heat transfer in the canister. In every axial position along the canister, three nodes are considered to calculate the wall temperature in the radial direction across the different layers. The model evaluates the conduction between the monolith and the canister by means of a thermal equivalence resistance between the last channel beam and the interface with the mat; the conduction across the solid layers (mat and metal can); the radiation, conduction, and convection in the air gap, if it exists; and the heat transfer by convection and radiation between the metal can and the environment. All the radial equivalent thermal resistances are defined in cylindrical coordinates. The axial conduction across the metal can and the thermal inertia of every node are also evaluated by means of the corresponding equivalent thermal resistances and capacities.

According to the nodal scheme of the canister, the wall temperature is calculated in every radial node as

$$T_{m,1}^{can^{p+1}} = \frac{\Delta t}{C_{m,1}^{can}}\left[\frac{T_{m,2}^{can^p} - T_{m,1}^{can^p}}{R_{m,1/m,2}^{can}} + \frac{T_{ext} - T_{m,1}^{can^p}}{R_{ext}^{can}} + \sum_{j=-1}^{1}\frac{T_{m+j,1}^{can^p} - T_{m,1}^{can^p}}{R_{m+j,1/m,1}^{can}}\right] + T_{m,1}^{can^p}, \tag{14}$$

$$T_{m,2}^{can^{p+1}} = \frac{\Delta t}{C_{m,2}^{can}} \left[\frac{T_{m,1}^{can^p} - T_{m,2}^{can^p}}{R_{m,1/m,2}^{can}} + \frac{T_{m,3}^{can^p} - T_{m,2}^{can^p}}{R_{m,3/m,2}^{can}} \right] + T_{m,2}^{can^p} \text{ and} \tag{15}$$

$$T_{m,3}^{can^{p+1}} = \frac{\Delta t}{C_{m,3}^{can}} \left[\frac{T_{m,2}^{can^p} - T_{m,3}^{can^p}}{R_{m,3/m,2}^{can}} + \frac{T_{m,2}^{H_{per}^p} - T_{m,3}^{can^p}}{R_{m,2}^{H_{per},can}} \right] + T_{m,3}^{can^p}, \tag{16}$$

where index j takes the values 1 and -1 and

$$R_{m,1/m,2}^{can} = R_{m,1/m,2(c)}^{can} + \frac{R_{m,1/m,2(gc)}^{can} R_{m,1/m,2(r)}^{can}}{R_{m,1/m,2(gc)}^{can} + R_{m,1/m,2(r)}^{can}}. \tag{17}$$

Additionally, the model considers the axial heat transfer due to conduction between the canister and the inlet and outlet cones of the DPF and between these and the inlet and outlet ducts, where the wall temperature is also calculated according to a nodal scheme [30]. It affects the specific formulation of the end nodes on the metal can (radial node 1) by adding the corresponding thermal equivalent resistance.

2.3. Formulation for fast wall temperature convergence

A properly calculation of heat transfer effects on the DPF response requires the knowledge of the initial wall temperature. However, it is not usually known. One of the reasons is the difficulty to define the initial values of the temperature distribution in the radial and axial directions; secondly, even known such temperature distribution from experimental data, it would be available for a limited number of operating conditions, since these data do not usually cover all the modelling range. As a consequence, an initial phase of temperature convergence is needed in the model. It causes an artificial increase of the computation time because of the thermal inertia effect controlling the time up to convergence.

To avoid this phase or even an incorrect calculation and prediction due to its omission, a formulation of the heat transfer equation based on neglecting the thermal inertia terms is proposed. For the sake of simplicity, this formulation is applied to the node on the interface between the porous wall and the gas flow in the outlet channel in Eq. (18). Given Eq. (13), the proposed formulation for fast convergence yields

$$\frac{T_{m,2}^{H^p} - T_{m,3}^{H^p}}{R_{m,3/m,2}^{H}} + \frac{T_{o}^{H^p} - T_{m,3}^{H^p}}{R_{o}^{H}} = 0. \tag{18}$$

If Eq. (18) is integrated during a characteristic cycle time (for example duration of an engine cycle, duration of a periodic signal under pulsating operation in flow test rig, arbitrary time under steady flow operation, etc.) and the wall

temperature and the equivalent thermal resistances due to conduction heat transfer are assumed to be constant during such a cycle, the wall temperature on node $(m,3)^H$ can be calculated as

$$\bar{T}^H_{m,3} = \frac{\frac{\bar{T}^H_{m,2} t_c}{R^H_{m,3/m,2}} + \sum_{p=1}^{n_p} \frac{T_o^{Hp} \Delta t^p}{R_o^{Hp}}}{\frac{t_c}{R^H_{m,3/m,2}} + \sum_{p=1}^{n_p} \frac{\Delta t^p}{R_o^{Hp}}}. \tag{19}$$

According to this formulation, the steady wall temperature in nodes $(m,1)^H$ and $(m,2)^H$ on the porous medium is obtained applying Eqs. (20) and (21) respectively:

$$\bar{T}^H_{m,1} = \frac{\frac{\bar{T}^H_{m,2} t_c}{R^H_{m,1/m,2}} + \sum_{p=1}^{n_p} \frac{T_i^{Hp} \Delta t^p}{R_i^{Hp}} + \sum_{p=1}^{n_p} \dot{q}^p_{chr} \Delta t^p}{\frac{t_c}{R^H_{m,1/m,2}} + \sum_{p=1}^{n_p} \frac{\Delta t^p}{R_i^{Hp}}} \tag{20}$$

$$\bar{T}^H_{m,2} = \frac{\sum_{j=-1}^{1} \frac{\bar{T}^H_{m+j,2} t_c}{R^H_{m+j,2/m,2}} + \sum_{h=-1}^{1} \frac{\bar{T}^{H+h}_{m,2} t_c}{R^{(H,H+h)^*}_{m,2}} + a}{\sum_{j=-1}^{1} \frac{t_c}{R^H_{m+j,2/m,2}} + \sum_{h=-1}^{1} \frac{t_c}{R^{(H,H+h)^*}_{m,2}} + b} \tag{21}$$

$$a = \sum_{p=1}^{n_p} \left(\frac{T_i^{Hp} \Delta t^p}{R_i^{Hp} + R^H_{m,1/m,2}} + \frac{T_o^{Hp} \Delta t^p}{R_o^{Hp} + R^H_{m,3/m,2}} \right) \tag{22}$$

$$b = \sum_{p=1}^{n_p} \left(\frac{\Delta t^p}{R_i^{Hp} + R^H_{m,1/m,2}} + \frac{\Delta t^p}{R_o^{Hp} + R^H_{m,3/m,2}} \right) \tag{23}$$

The solution is implicit because of the heat transfer between adjacent channel beams and in the axial direction taking place in radial node 2, so that the system is solved iteratively. At the end of every cycle, the initial value for $\bar{T}^H_{m,2}$ is obtained in every axial node of every channel beam assuming that there is not heat transfer in the axial direction or with the adjacent channel beams. Afterwards, the value of $\bar{T}^H_{m,2}$ in every axial node of every channel beam is obtained applying iteratively Eq. (21). The convergence is defined by a threshold equal to 0.02% in every node $(m,2)^H$.

With respect to the canister wall temperature, the fast convergence formulation yields

$$\bar{T}^{can}_{m,1} = \frac{\frac{T_{ext} t_c}{R^{can}_{ext}} + \frac{\bar{T}^{Hper}_{m,2} t_c}{R^{can}_{m,1/m,2} + R^{can}_{m,3/m,2} + R^{Hper,can}_{m,2}} + \sum_{j=-1}^{1} \frac{\bar{T}^{can}_{m+j,1} t_c}{R^{can}_{m+j,1/m,1}}}{\frac{t_c}{R^{can}_{ext}} + \frac{t_c}{R^{can}_{m,1/m,2} + R^{can}_{m,3/m,2} + R^{Hper,can}_{m,2}} + \sum_{j=-1}^{1} \frac{t_c}{R^{can}_{m+j,1/m,1}}}; \tag{24}$$

$$\bar{T}^{can}_{m,2} = \frac{\frac{T_{ext} t_c}{R^{can}_{ext} + R^{can}_{m,1/m,2}} + \frac{\bar{T}^{Hper}_{m,2} t_c}{R^{can}_{m,3/m,2} + R^{Hper,can}_{m,2}}}{\frac{t_c}{R^{can}_{ext} + R^{can}_{m,1/m,2}} + \frac{t_c}{R^{can}_{m,3/m,2} + R^{Hper,can}_{m,2}}}; \tag{25}$$

$$\overline{T}^{can}_{m,3} = \frac{\frac{T_{ext} t_c}{R^{can}_{ext}+R^{can}_{m,1/m,2}+R^{can}_{m,3/m,2}} + \frac{\overline{T}^{H_{per}}_{m,2} t_c}{R^{H_{per}.can}_{m,2}}}{\frac{t_c}{R^{can}_{ext}+R^{can}_{m,1/m,2}+R^{can}_{m,3/m,2}} + \frac{t_c}{R^{can}_{m,3/m,2}+R^{H_{per}.can}_{m,2}}}. \tag{26}$$

This system is also solved iteratively. In this case, the wall temperature on the external surface includes radial and axial heat transfer conduction, so that the solution in every node $(m, 1)^{can}$ requires the convergence in every axial node m. Additionally, the canister wall temperature in the radial direction depends on the environment temperature and the wall temperature of radial node 2 located in the porous wall of the peripheral channel beam. As a consequence, the wall temperature on the peripheral channel beam and on the canister is solved in a combined iterative process governed by the convergence of $\overline{T}^{H_{per}}_{m,2}$ and $\overline{T}^{can}_{m,1}$ in every axial node m.

2.4. Heat transfer model parameters

The prediction capabilities of the proposed model depend on its formulation but also on the definition of the involved heat transfer parameters. The heat transfer coefficient inside the channels is calculated according to a correction of the correlation proposed by Vortruba [31], whose value is reduced an 80%. The Churchill & Berstein's heat transfer coefficient [32] adding the radiation heat transfer coefficient is applied to account for the solid to gas phase heat transfer on the canister surface.

The material properties are set according to the DPF characteristics. Table 1 summarises the heat transfer input parameters for ceramics and canister materials inside the experimental temperature range.

Table 1 indicates the properties for sinterized silicon carbide. These magnitudes need to be corrected with the porosity in order to define the substrate properties including the gas phase:

$$\rho_s = (1-\varepsilon)\,\rho_{\mathrm{SiC}} + \varepsilon\rho_g \tag{27}$$

$$c_{p_s} = (1-\varepsilon)\,c_{p_{\mathrm{SiC}}} + \varepsilon c_{p_g} \tag{28}$$

$$k_s = (1-\varepsilon)\,k_{\mathrm{SiC}} + \varepsilon k_g \tag{29}$$

In the case of the existence of a particulate layer on the porous walls of the inlet channels, the thermal properties of this layer are calculated according to Eqs. (27), (28) and (29) but considering the properties of primary soot particles as solid porous substrate [23]. The influence of soot deposits inside the porous wall have been neglected in the heat transfer modelling.

Eq. (29) provides the porous substrate conductivity, which is applied in the tangential and axial direction of an isolate porous wall according to the nodal scheme shown in Figure 1. In order to account for radial heat transfer across the monolith cross section, i.e. to determine the thermal equivalent resistance between adjacent channels, it is applied the continuum approximation of heat conduction in the unit cell of honeycomb monoliths reactors proposed

by Groppi and Tronconi [21]. This approach has been adapted in this work to wall-flow DPF monoliths because of the existence of a particulate layer on the inlet channels walls. In this case, the characteristic inlet and outlet unit cells are shown in Figure 5. The cementation between segments composing SiC monoliths is neglected.

Considering the parameters that define the characteristic inlet and outlet unit cells, the effective radial conductivity in a honeycomb wall-flow monolith can be expressed as

$$k_r = \left(\frac{w_w}{k_s\left(\alpha + w_w\right)} + \frac{4 w_p k_s k_{p_{th}} k_g}{\left(k_s k_{p_{th}}^2 k_g + k_s k_{p_{th}} k_g^2\right)\alpha + 2 k_s^2 k_{p_{th}} k_g w_w} + \frac{\alpha - 2w_p}{k_s w_w + k_{p_{th}} w_p + k_g\left(\alpha - w_p\right)} \right)^{-1}. \tag{30}$$

Eq. (30) shows the dependence of the effective radial conductivity on the substrate conductivity, which is in turn function of the substrate porosity, as previously shown in Eq. (29). Plot (a) in Figure 6 represents the variation of the effective radial conductivity as function of the temperature, which affects the substrate conductivity, and the substrate porosity. Clean and loaded (10 g/L) DPF conditions are considered for every substrate porosity finding a slightly higher effective radial conductivity in the case of loaded DPF. The reason is the low thermal conductivity of soot and the thickness of the particulate layer, which is two and three orders of magnitude lower than porous wall thickness (w_w) and cell size (α) respectively.

On the other hand, plot (b) in Figure 6 represents the variation of the effective radial conductivity for different open frontal area (OFA) (calculated considering inlet and outlet channels open area) of the wall-flow DPF. The substrate porosity and the soot loading are 0.45 and 10 g/L respectively independently of the OFA. Due to the low gas conductivity, the design of adiabatic DPF monoliths requires high OFA. Nevertheless, it may lead to lower mechanical integrity and the appearance of hot spots in operating conditions at low flow rates. This is a trade-off specially important in pre-turbo DPF configurations regarding mechanical loads, since it can be significantly higher than in its traditional post-turbo placement in the exhaust line. The higher mean thermal level would be favourable in the pre-turbo DPF configuration; the expected quasi-continuous regeneration would lead to thermal balance along the monolith and would contribute to avoid hot spots appearance due to partial regeneration and uncontrolled light-off.

3. Experimental validation

The validation of the wall-flow DPF heat transfer model has been performed through the comparison with experimental data obtained in a hot flow test rig. The tests have covered clean and loaded DPF, continuous flow under steady and transient thermal conditions, and pulsating flow.

3.1. Experimental facility

Figure 7 shows schematically the layout of the continuous and pulsating flow test rig designed by CMT-Motores Térmicos [36] in which the tests for the study of the heat transfer phenomena in wall-flow DPFs have been performed. The characteristics of the DPF used in the validation of the proposed heat transfer model are summarised in Table 2.

In the test rig the air is pumped into the DPF by means of a 55 kW screw compressor. Next the air flows through a set of 5 electric heaters, which can heat the air flow up to 673 K. Because of heating due to compression process, the test rig has also available a heat exchanger to carry out tests at controlled low temperature. A rotary valve has been used in order to generate pulsating flow at the DPF inlet simulating inflow conditions when the DPF is coupled with an engine and placed both upstream or downstream of the turbine. The rotary valve design allows controlling pulse frequency and amplitude.

A series of sensors are also installed in order to record experimental data according to the layout shown in Figure 8. Type K thermocouples are used to record gas and canister wall temperature. The air temperature is measured in the inlet and outlet ducts of the DPF by installing four thermocouples in the same cross section of each duct at 0.9 m from the DPF. Regarding the DPF, three thermocouples are placed inside the outlet channels in order to measure the radial flow temperature distribution. The temperature on the DPF canister is measured by means of three thermocouples located along the monolith length.

The instantaneous static pressure fluctuations of the pulsating flow are measured by means of two piezoresistive KISTLER sensors with a measuring range of $0-5$ bar, which are installed 0.95 m before and after the DPF. The average flow static pressure is also measured at the inlet and outlet of the DPF by means of piezometric rings coupled with average pressure KISTLER sensors with a measuring range of $0-5$ bar.

Finally, an ABB hot-film anemometer is used to record the air mass flow. Its measuring range is $0-720$ kg/h with a maximum error equal to $\pm 1\%$. It is installed at the outlet of the measuring line after a heat exchanger cooling the air up to the environment temperature.

3.2. Results and discussion

The first stage of the test campaign to assess the ability of the heat transfer model considers continuous flow at 523 K. Figure 9(a) shows the comparison between the measured outlet gas temperature at different mass flows versus the predicted value provided by the model with different number of channel beams.

The error in outlet gas temperature prediction is shown in Figure 9(b). It is a relative error referred to the range of temperature in which is performed the prediction of the model. Therefore, it has been calculated as the difference between the modelled and the experimental temperature divided into the temperature range defined by the boundaries of the test; i.e. the inlet gas temperature, which represents the hot focus, and the ambient temperature, which represents the cold focus:

$$Error = \frac{T_{mod} - T_{exp}}{T_{in} - T_{amb}} \tag{31}$$

The results show the high accuracy provided by the model in the prediction of the outlet gas temperature whatever the number of channel beams, although the error slightly increases as the mass flow rate decreases and the number of channel beams is reduced. It confirms the suitability of the use of the model in comprehensive engine gas dynamic calculations with the solution of only one pair of inlet and outlet channels (1 channel beam). This is a very extended assumption to save computational effort. However, it also usually means not considering heat exchange with the ambient and hence overpredicting the outlet gas temperature [37]. The proposed model overcomes this problem, which is critic when applied to the analysis of pre-turbo DPF configurations due to the fact that the DPF outlet temperature defines the available energy for the turbine [12, 16].

A more detailed analysis of the DPF thermal behaviour demands the use of several channel beams. Plot (a) in Figure 10 represents the gas temperature inside the outlet channels at 0.09 m from its plug ends as function of its radial location. The clear increase of outlet gas temperature as the mas flow rate increases (also shown in Figure 9) confirms the prevalence of conduction, and hence residence time, over convection as main heat exchange phenomenon.

The use of 10 channel beams (1.32 cm in radial mesh) provides a very detailed and accurate prediction of in-monolith gas temperature. It validates the wall temperature prediction, which in fact controls the regeneration rate [38]. Figure 10(b) shows that the wall temperature drop with respect to the monolith core reaches 50 K at the canister-monolith interface even with low inlet gas temperature (523 K) and increasing as the mass flow rate decreases. Figure 11 shows the wall temperature field at high pulsating mass flow (375 kg/h, amplitude 0.3 bar and frequency 66.6 Hz) and higher inlet gas temperature (T_{in} = 643 K). As expected, the radial temperature drop is higher than in previous cases in Figure 10(b) because of the greater gradient with respect to the environment temperature. The temperature drop in the axial direction is shown to be negligible with respect to the radial conduction effect. The sharp radial decrease rate points out its potential influence on conclusions about soot reactivity, regeneration ignition point, hot spots prediction, etc. The need of converging towards models able to take into account this effect being coupled at the same time with porous and channel scale solution has been addressed in works regarding regeneration modelling [14].

The results have also shown the capability to predict the canister wall temperature, whose main interest lies on thermal insulation design, EGR pre-cooling analysis in multi-functional exhaust manifolds [39, 40] and heat recovery DPF designs [41]. Figure 12 shows that it can be accurately predicted even with a rough radial mesh (4 channel beams). In this way, the thermal coupling between the DPF and the inlet and outlet ducts allows obtaining the parabolic profile of the canister wall temperature. The temperature gradient between the ends and the centre of the DPF advises the use of high conduction materials to avoid external undistributed thermal loads able to affect the mat binding.

Table 3 shows the outlet gas temperature predicted by the model for several mass flows under hot pulsating flow operation and its comparison with experimental data. The pulse frequency is 66.6 Hz for all the considered operating points and corresponds to 2000 rpm in a four cylinder engine. The pulse amplitude is 0.3 bar, which falls into the order of magnitude for pre-turbo aftertreatment exhaust manifolds [16]. The maximum error in outlet gas temperature prediction is scarcely higher than 1% independently of the soot loading, mass flow and inlet gas temperature.

Both the modelled and the experimental data corresponding to operating points with loaded DPF show the slight influence of soot loading despite its high value equal to 22 g/L. The soot loading produces a gas temperature decrease around 2 K for this pulse amplitude and frequency. This result is sound with effective radial conductivity proposed in Eq. (30), which indicates a slight increase of its value when appears the particulate layer and provides the model the ability to reproduce its effect on heat transfer.

Table 4 also shows the effect of the soot loading, which appears whatever the pulse amplitude and frequency. The difference in outlet gas temperature between clean and loaded DPF is again around 2 K both for experimental and modelled data. The parametric study varying pulse amplitude and frequency leads to conclude that frequency has not influence on heat exchange. However, the increase of pulse amplitude reduces the gas to solid heat exchange. Although the increase in temperature is also reduced in this case, the proposed heat transfer model and its coupling with an unsteady compressible flow solver shows the sensitivity to properly reproduce this phenomenon.

Finally, Figure 13 is devoted to the analysis of the model ability during thermal transient operation, both warm-up and cooling. The modelling of thermal transients is relevant for DPF modelling itself as independent element but becomes key in comprehensive engine simulations with pre-turbo aftertreatment configuration because of the coupling with the turbocharger operation [12, 16] or in whole aftertreatment lines with SCR systems downstream of the DPF.

Three tests were carried out under steady mass flow conditions. The comparison between experimental and modelled results is represented in separated plots for warm-up in Figure 13(a) and cooling in Figure 13(b). The duration of the thermal transients is mainly depending on the facility management and thermal inertia, specially that of the electric heaters. It makes not possible to impose a sudden step in inlet temperature. Other factors affecting the duration of the process is the maximum inlet temperature and DPF loading ($T_{in_{max}}$; Test 1 at 661 K and clean DPF; Test 2 at 588 K and clean DPF; Test 3 at 573 K and loaded DPF (22 g/L)) and the mass flow (375 kg/h in the case of Test 1 and 200 kg/h in Tests 2 and 3).

The simulations have been carried out imposing to the model the inlet gas temperature in the inlet duct. For the sake of simplicity, only the case of Test 1 is represented. Only 1 channel beam has been applied in the radial discretisation in order to reduce the computational effort. Results in Figure 13 confirms the ability of the heat transfer model to predict with good accuracy the outlet gas temperature during the performed tests both in heating and cooling processes.

4. Summary and conclusions

A heat transfer model for honeycomb wall-flow DPFs has been presented in this paper. The proposed model is based on the bi-dimensional discretisation of the porous medium between the inlet and the outlet channels of the monolith. Additionally, the monolith can be discretised in the radial direction by means of concentric channel beams where all the pairs of inlet and outlet channels are assumed to behave the same. It is proposed the coupling between the concentric beams in order to account for the conductive heat transfer in the radial direction. Finally, the monolith radial mesh is connected with the DPF canister, where a specific bi-dimensional discretisation is also proposed. It allows providing the wall and gas temperature field in the DPF, assuming axysimmetric behaviour and including both the monolith and the canister.

The equivalent thermal resistance scheme of the porous medium is able to take into account the existence of a particulate layer and its effect on the effective radial conductivity. A theoretical expression to calculate it has been proposed based on the representative unit cell in wall-flow monoliths. Given a substrate material, the effective radial conductivity depends mainly on the open frontal area of the monolith, the substrate porosity and the wall temperature. The existence of the particulate layer produces a slight increase of the radial conductivity. This theoretical result has been confirmed by experimental data and by the model prediction, which has been shown highly sensitive to the particulate layer effect leading to a slight decrease of the outlet gas temperature.

The DPF is usually placed downstream of the turbine, where the flow is essentially quasi-steady. Nevertheless, an increasing interest for pre-turbo aftertreatment configurations is demanding the capability to model thermo-and fluid dynamic DPF behaviour under unsteady pulsating flow. In this way, the model validation has been conducted under steady and pulsating flow. Results have confirmed the dominant effect of conductive heat exchange over convective phenomena in wall-flow monoliths, as found in through-flow chemical reactors. Residence time is one of the main parameters controlling heat losses in the DPF, so that the ratio length to diameter gets more importance in pre-turbo DPF configurations. As this ratio decreases for the same cellular geometry and filtration area, the pressure drop and the external surface are reduced. However, the residence time is almost constant and the mechanical durability increases as the aspect ratio tends to 1. Since thermal losses have great importance in pre-turbo aftertreatment configurations, the filtration area may be approached to be reduced to lead to lower residence time and external surface. This strategy would contribute to higher temperature at the inlet of the turbine but at the expense of increasing pressure drop and reducing ash accumulation capacity defining a trade-off governing the design process.

With respect to the influence of flow characteristics on model performance, results show high agreement with experimental data both in the monolith, canister and outlet of the DPF. In the case of operation under pulsating flow, it has been found that frequency has not influence on outlet gas temperature but the increase of the pulse amplitude slightly reduces heat losses for the same mass flow and mean inlet temperature. Reasons can be found in the reduction of the effective residence time because of the higher instantaneous velocities.

Appendix A: Gas phase governing equations

The wall-flow DPF model solves the flow across the canned DPF device. The governing equations inside the monolith channels are formulated for non-homentropic one-dimensional unsteady compressible flow [19]:

- Mass conservation

$$\frac{\partial\left(\rho_j F_j\right)}{\partial t} + \frac{\partial\left(\rho_j u_j F_j\right)}{\partial x} = (-1)^j 4\left(\alpha - 2w_p j\right)\rho_j u_{w_j} \tag{32}$$

- Momentum conservation

$$\frac{\partial\left(\rho_j u_j F_j\right)}{\partial t} + \frac{\partial\left(\rho_j u_j^2 F_j + p_j F_j\right)}{\partial x} - p_j \frac{dF_j}{dx} = -F_w \mu_j u_j \tag{33}$$

- Energy conservation

$$\frac{\partial\left(e_{0j}\rho_j F_j\right)}{\partial t} + \frac{\partial\left(h_{0j}\rho_j u_j F_j\right)}{\partial x} = q_j \rho_j F_j + (-1)^j 4\left(\alpha - 2w_p j\right) h_{0w}\rho_j u_{w_j} \tag{34}$$

Subscript j in Eqs. (32)-(34) identifies the type of monolith channel. It takes value 0 for the solution of the outlet channels and value 1 in the case of the inlet channels.

The conservation equations system in a pair of inlet and outlet channels is closed by the state equation for an ideal gas in every one of the channels and the equation governing the pressure drop across the porous medium. It allows obtaining the value of the filtration velocity [19]. The solution of the boundary conditions is described in detail in [28].

Acknowledgements

This work has been partially supported by the spanish Ministerio de Ciencia e Innovación through grant number DPI2010-20891-C02-02.

References

[1] O. Salvat, P. Marez, G. Belot, Passanger car serial application of a particulate filter system on a common-rail, direct-injection Diesel engine, in: SAE Technical Paper 2000-01-0473, 2000.

[2] W. Knecht, Diesel engine development in view of reduced emission standards, Energy 33 (2) (2008) 264–271.

[3] F. Payri, V. Bermúdez, R. Payri, F. J. Salvador, The influence of cavitation on the internal flow and the spray characteristics in diesel injection nozzles, Fuel 83 (4-5) (2004) 419–431.

[4] J. M. Desantes, V. Bermúdez, J. M. García, E. Fuentes, Effects of current engine strategies on the exhaust aerosol particle size distribution from a heavy-duty Diesel engine, Journal of Aerosol Science 36 (10) (2005) 1251–1276.

[5] A. J. Torregrosa, A. Broatch, R. Novella, L. F. Mónico, Suitability analysis of advanced diesel combustion concepts for emissions and noise control, Energy 36 (2) (2011) 825–838.

[6] J. R. Serrano, F. J. Arnau, V. Dolz, P. Piqueras, Methodology for characterization and simulation of turbocharged Diesel engines combustion during transient operation. Part 1: Data acquisition and post-processing, Applied Thermal Engineering 29 (1) (2009) 142–140.

[7] J. R. Serrano, H. Climent, C. Guardiola, P. Piqueras, Methodology for characterisation and simulation of turbocharged Diesel engines combustion during transient operation. Part 2: Phenomenological combustion simulation, Applied Thermal Engineering 29 (1) (2009) 150–158.

[8] C. D. Rakopoulos, A. M. Dimaratos, E. G. Giakoumis, D. C. Rakopoulos, Evaluation of the effect of engine, load and turbocharger parameters on transient emissions of Diesel engine, Energy Conversion and Management 50 (9) (2009) 2381–2393.

[9] C. D. Rakopoulos, A. M. Dimaratos, E. G. Giakoumis, D. C. Rakopoulos, Investigating the emissions during acceleration of a turbocharged Diesel engine operating with bio-diesel or n-butanol diesel fuel blends, Energy 35 (12) (2010) 5173–5184.

[10] A. Sarvi, R. Zevenhoven, Large-scale Diesel engine emission control parameters, Energy 35 (2) (2010) 1139–1145.

[11] V. Bermúdez, J. M. Luján, B. Pla, W. G. Linares, Effects of low pressure exhaust gas recirculation on regulated and unregulated gaseous emissions during NEDC in a light-duty Diesel engine, Energy 36 (9) (2011) 5655–5665.

[12] V. Bermúdez, J. R. Serrano, P. Piqueras, O. García-Afonso, Influence of DPF soot loading on engine performance with a pre-turbo aftertreatment exhaust line, in: SAE Technical Paper 2012-01-0362, 2012.

[13] S. J. Lee, S. J. Jeong, W. S. Kim, Numerical design of the diesel particulate filter for optimum thermal performances during regeneration, Applied Energy 86 (7-8) (2009) 1124–1135.

[14] S. Bensaid, D. L. Marchisio, D. Fino, Numerical simulation of soot filtration and combustion within diesel particulate filters, Chemical Engineering Science 65 (1) (2010) 357–363.

[15] J. Honeder, N. Ardey, M. Kaufmann, T. Steinmayr, The new BMW 4-/6- cylinder Diesel engine with 2-stage turbocharging, in: 20th Aachen Colloquium "Automobile and Engine Technology", 2011.

[16] V. Bermúdez, J. R. Serrano, P. Piqueras, O. García-Afonso, Assessment by means of gas dynamic modelling of a pre-turbo diesel particulate filter configuration in a turbocharged HSDI Diesel engine under full-load transient operation, Proceedings of the Institution of Mechanical Engineers, Part D: Journal of Automobile Engineering 225 (9) (2011) 1134–1155.

[17] F. Payri, J. R. Serrano, P. Piqueras, O. García-Afonso, Performance analysis of a turbocharged heavy duty Diesel engine with a pre-turbo diesel particulate filter configuration, SAE Int. J. Engines 4 (2) (2011) 2559–2572.

[18] C. Brüstle, M. Downey, M. N. Subramaniam, A. Birckett, D. Tomazic, Aftertreatment in a pre-turbo position: size and fuel consumption advantage for Tier 4 large-bore Diesel engines, in: Aachen Colloquium Automobile and Engine Technology 2011, 2011.

[19] A. J. Torregrosa, J. R. Serrano, F. J. Arnau, P. Piqueras, A fluid dynamic model for unsteady compressible flow in wall-flow diesel particulate filters, Energy 36 (1) (2011) 671–684.

[20] F. Payri, A. Broatch, J. R. Serrano, P. Piqueras, Experimental-theoretical methodology for determination of inertial pressure drop distribution and pore structure properties in wall-flow diesel particulate filters (DPFs), Energy 36 (12) (2011) 6731–6744.

[21] G. Groppi, E. Tronconi, Continuous vs. discrete models of non-adiabatic monolith catalyst, AIChE Journal 42 (8) (1996) 2382–2387.

[22] G. Groppi, E. Tronconi, Design of novel monolith catalyst supports for gas/solid reactions with heat exchange, Chemical Engineering Science 55 (12) (2000) 2161–2171.

[23] O. A. Haralampous, G. C. Koltsakis, Intra-layer temperature gradients during regeneration of diesel particulate filters, Chemical Engineering Science 57 (13) (2002) 2345–2355.

[24] C. K. Dardiotis, O. A. Haralampous, G. C. Koltsakis, Catalytic oxidation performance of wall-flow versus flow-through monoliths for diesel emissions control, Industrial and Engineering Chemistry Research 45 (10) (2006) 3520–3530.

[25] C. K. Dardiotis, O. A. Haralampous, G. C. Koltsakis, Catalytic oxidation in wall-flow reactors with zoned coating, Chemical Engineering Science 63 (4) (2008) 1142–1153.

[26] M. Schejbal, M. Marek, M. Kubicek, P. Kocia, Modelling of diesel filters for particulates removal, Chemical Engineering Journal 154 (2009) 219–230.

[27] M. Schejbal, J. Stepanek, M. Marek, P. Kocia, M. Kubicek, Modelling of soot oxidation by NO_2 in various types of diesel particulate filters, Fuel 89 (9) (2010) 2365–2375.

[28] J. M. Desantes, J. R. Serrano, F. J. Arnau, P. Piqueras, Derivation of the method of characteristics for the fluid dynamic solution of flow advection along porous wall channels, Applied Mathematical Modelling 36 (2012) 3134–3152.

[29] C. Ilikali, M. Çetin, S. Çetin, Methods for the freezing time in ellipses, Journal of Food Engineering 28 (3-4) (1996) 361–372.

[30] J. Galindo, J. M. Luján, J. R. Serrano, V. Dolz, S. Guilain, Description of a heat transfer model suitable to calculate transient processes of turbocharged Diesel engines with one-dimensional gas-dynamic codes, Applied Thermal Engineering 26 (1) (2006) 66–76.

[31] J. Vortruba, O. Mikus, K. Nguen, V. Hlavacek, J. Skrivanek, Heat and mass transfer in honeycomb catalysts – II, Chemical Engineering Science 30 (2) (1975) 201–206.

[32] S. W. Churchill, M. Bernstein, A correlating equation for forced convection from gases and liquids to a circular cylinder in crossflow, Journal of Heat Transfer 99 (2) (1977) 300–306.

[33] Ceramics WebBook, NIST Property Data Summaries, www.ceramics.nist.gov (2012).

[34] Thermal Ceramics, Division of the Morgan Crucible Company, UK, www.thermalceramics.com (2012).

[35] J. Holman, Transferencia de calor, McGraw-Hill, Interamericana de España, 1998.

[36] CMT-Motores Térmicos, Universitat Politècnica de València. www.cmt.upv.es (2012).

[37] M. N. Subramaniam, V. Joergl, P. Keller, O. Weber, T. Toyoshima, C. D. Vogt, Feasibility assessment of a pre-turbo after-treatment system with a 1D modeling approach, in: SAE Technical Paper 2009-01-1276, 2009.

[38] E. J. Bisset, Mathematical model of the thermal regeneration of a wall-flow monolith diesel particulate filter, Chemical Engineering Science 39 (7-8) (1984) 1233–1244.

[39] F. Payri, J. M. Desantes, J. Galindo, J. R. Serrano, Exhaust manifold of a turbo-supercharged reciprocating engine, Patent application P200900482. Priority date 13/02/2009. Oficina Española de Patentes y Marcas (2009).

[40] F. Payri, J. M. Desantes, P. Piqueras, J. R. Serrano, Dispositive for treatment of exhaust gases from Diesel turbo-supercharged internal combustion engines, Patent application P201131537. Priority date 23/09/2011. Oficina Española de Patentes y Marcas (2011).

[41] D. Zarvalis, N. Vlachos, S. Lorentzou, A.G. Konstandopoulos, Development of a multi-functional reactor with integrated heat recovery capability, in: Proceedings of GPC 2009, Vol. 53 [CD-ROM], Global Powertrain Congress, Vaals, The Netherlands, June 23-24, 2009.

Nomenclature

A	Amplitude
c_p	specific heat capacity
C	equivalent thermal capacity
D	diameter
e_0	specific stagnation internal energy
F	area
F_w	momentum transfer coefficient for square channels
Fr	frequency
h	heat transfer coefficient
h_0	specific stagnation enthalpy
k	thermal conductivity
k_g	gas thermal conductivity
k_p	particulate layer permeability
k_{pth}	particulate layer thermal conductivity
k_r	effective radial thermal conductivity
k_s	substrate thermal conductivity
k_w	porous wall permeability
l	length
p	pressure
q	heat per unit of time and mass
$\dot{q}_{chr}$	heat per unit of time
$\dot{q}''_{chr}$	heat per unit of time and volume
R	equivalent thermal resistance
S	surface
t	time dimension
t_c	cycle duration
T	temperature
T_{in}	inlet gas temperature
T_{out}	outlet gas temperature
$\bar{T}$	steady wall temperature
u	velocity
u_w	filtration velocity
V	volume

w_p	particulate layer thickness
w_w	porous wall thickness
x	axial dimension
z	tangential dimension

Greek letters

α	honeycomb cell size
Δt	time-step
Δx	axial mesh
Δz	tangential mesh
ϵ	emissivity
ε	porosity
μ	dynamic viscosity
ρ	density
σ	cell density

Subscripts

amb	ambient
c	metal can
cond	conduction
conv	convection
exp	experimental
ext	external
g	gas
gc	air gap conduction
ht	heat transfer
i	inlet channel
ini	initial
int	internal
m	index for node in the axial direction
max	maximum
mod	modelled
n	index for node in the tangential direction
o	outlet channel

p	particulate layer
per	peripheral
r	radiation
s	substrate

Superscripts

*	corrected
can	canister
H	index for channel beam
p	time instant
n_p	number of calculated time instants in a cycle

Abbreviations

DPF	diesel particulate filter
OFA	open frontal area
SCR	selective catalytic reduction

List of Tables

List of Figures

Table 1: Thermal properties of DPF materials.

Material	ρ [kg/m^3]	c_p [J/kgK]	k [W/mK]	ϵ [−]
Ceramics (SiC) [33]	3100	806-955	100-81	
Mat [34]	96	1050	0.06	0.06
Metal can [35]	7816	460	17	0.104

Table 2: Geometrical characteristics of the DPF.

Length	[m]	0.2
Diameter	[m]	0.132
Plug length	[mm]	3.2
Wall permeability	[m^2]	2.49e-13
Porosity	[%]	41.5
Mean pore diameter	[μm]	12
Cell density	[cpsi]	200
Filter cell size	[mm]	1.486
Number of channels	[−]	4246
Filtration area	[m^2]	2.5
Inlet cone volume	[cm^3]	500
Outlet cone volume	[cm^3]	450

Table 3: Outlet gas temperature prediction as function of the soot loading, mass flow and inlet gas temperature. Steady thermal operation with pulsating flow characterised by 0.3 bar in amplitude and 66.6 Hz in frequency. Calculation with 10 channel beams.

		Clean DPF			Loaded DPF		
Mass flow	T_{in}	T_{out}		Error	T_{out}		Error
		Exp.	Mod.		Exp.	Mod.	
[kg/h]	[K]	[K]	[K]	[%]	[K]	[K]	[%]
250	523	508.4	507.8	-0.28	504.4	505.5	0.50
375	523	512.4	511.7	-0.32	510.5	510.7	0.09
375	643	624.4	620.8	-1.07			

Table 4: Outlet gas temperature prediction as function of soot loading and pulsating flow characteristics (amplitude and frequency). Steady thermal operation with pulsating flow at T_{in} = 523 K and $\dot{m}$ = 375 kg/h. Calculation with 10 channel beams.

		Clean DPF			Loaded DPF		
Fr	A	T_{out}		Error	T_{out}		Error
		Exp.	Mod.		Exp.	Mod.	
[Hz]	[bar]	[K]	[K]	[%]	[K]	[K]	[%]
	0.5	512.9	515.2	1.06	510.7	510.4	-0.14
33.3	0.3	512.2	512.9	0.32	510.5	510	-0.23
	0.12	511	510.5	-0.23	509	508.8	-0.09
	0.5	514.4	513.3	-0.50	510.8	510.2	-0.28
66.6	0.3	512.4	511.7	-0.32	510.5	510.7	0.09
	0.12	510.8	510.5	-0.14	509	508.9	-0.05
	0.5	512.9	512.1	-0.37	510.6	510.7	0.05
100	0.3	511.7	510.9	-0.37	510.1	510.2	0.05
	0.12	510.8	510.9	0.05	508.9	509.3	0.18

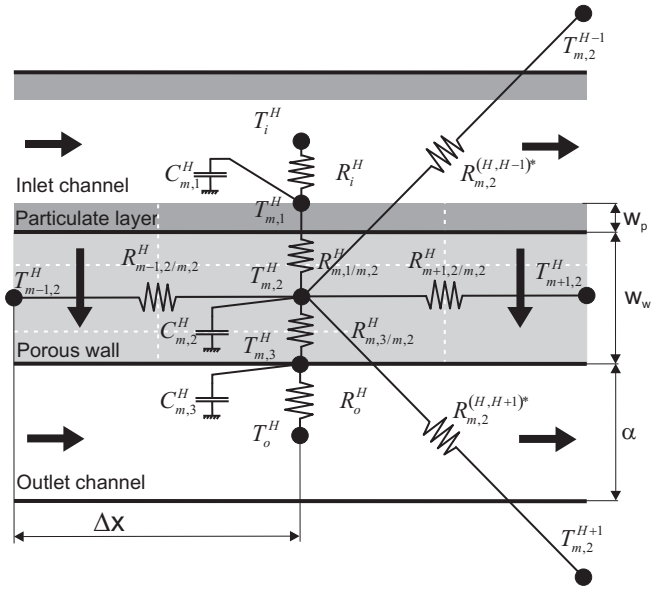

Figure 1: Nodal scheme on porous wall for channel wall temperature calculation.

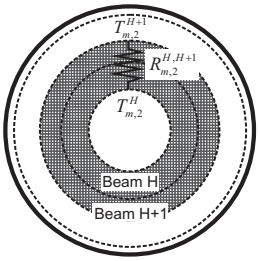

Figure 2: Approach for equivalent thermal resistance calculation between adjacent channel beams.

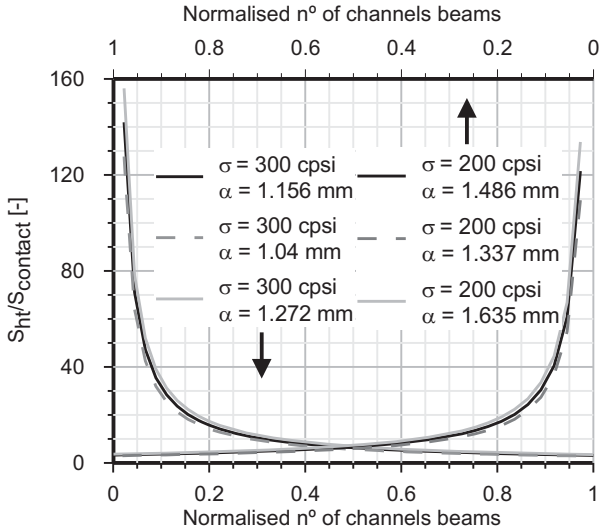

Figure 3: Corrector factor value for radial equivalent thermal resistances between adjacent channel beams: influence of the cellular geometry and the normalised number of channel beams.

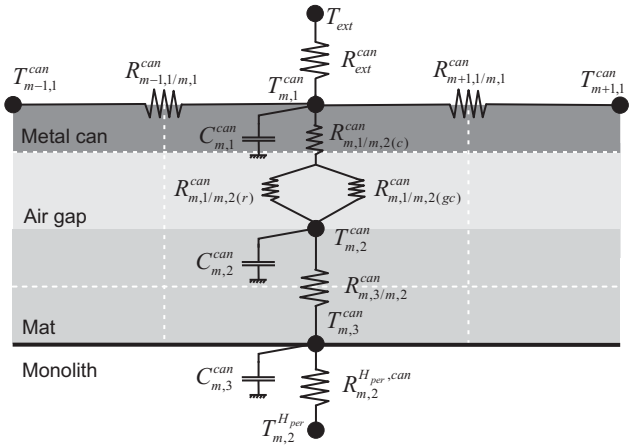

Figure 4: Nodal scheme on the canister for external wall temperature calculation.

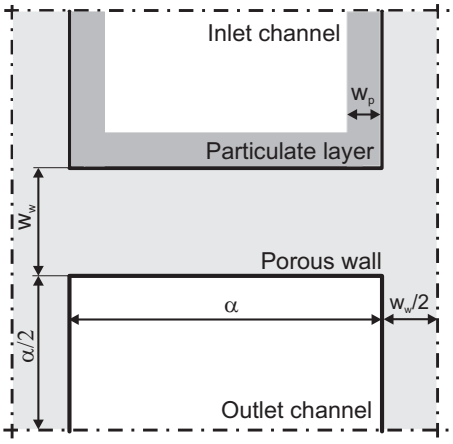

Figure 5: Cross section of the characteristic inlet and outlet unit cells in loaded wall-flow DPF monoliths.

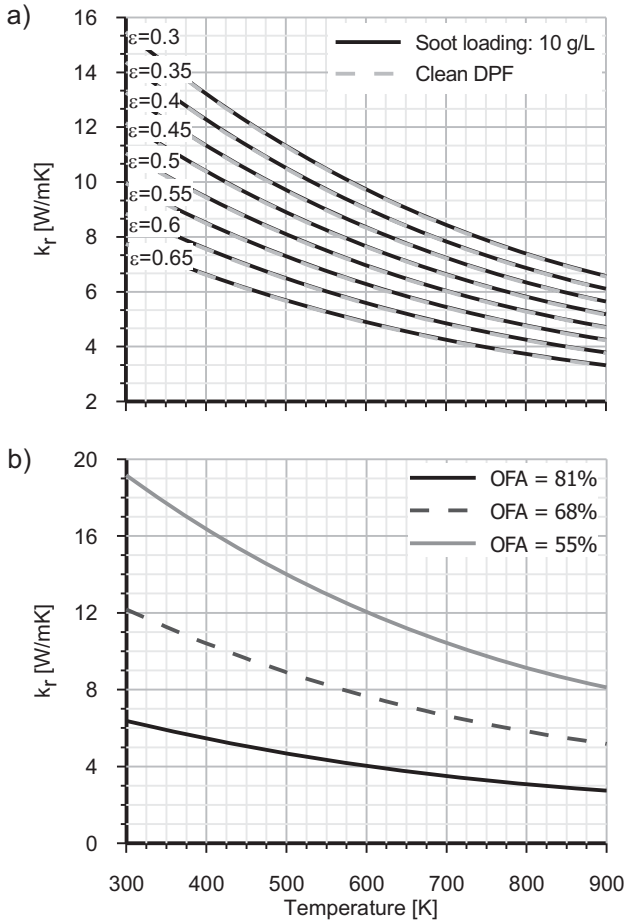

Figure 6: Effective radial conductivity: dependence on (a) porosity and (b) open frontal area.

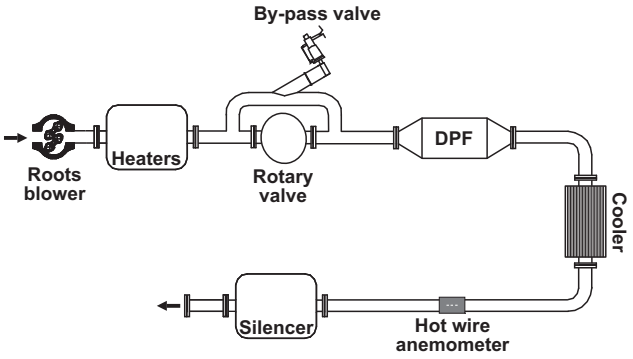

Figure 7: Scheme of the experimental flow test rig.

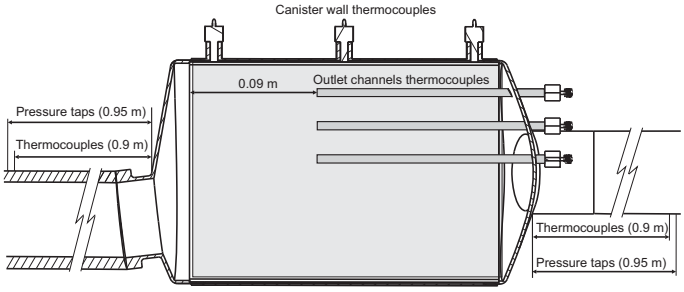

Figure 8: Layout of pressure and temperature sensors in the test rig.

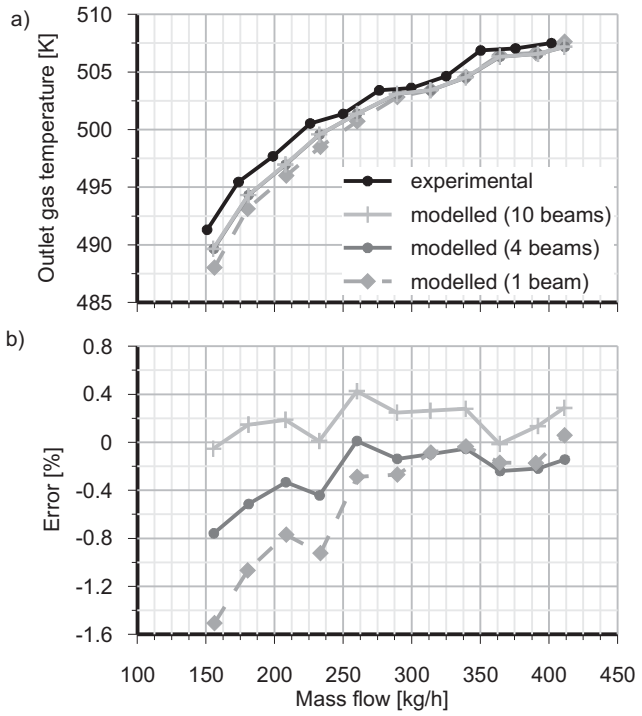

Figure 9: Outlet gas temperature prediction. Steady thermal operation with steady flow at T_{in} = 523 K and DPF soot loading equal to 22 g/L.

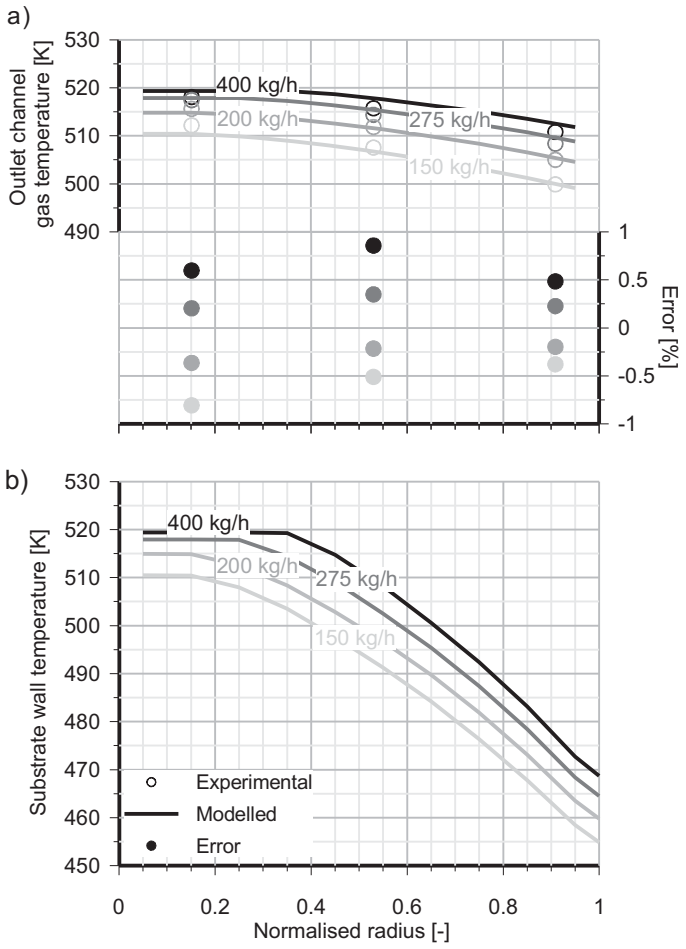

Figure 10: Outlet channel gas and substrate wall temperature prediction at 0.09 m from the channel plug end. Steady thermal operation with steady flow at T_{in} = 523 K and DPF soot loading equal to 22 g/L. Calculation with 10 channel beams.

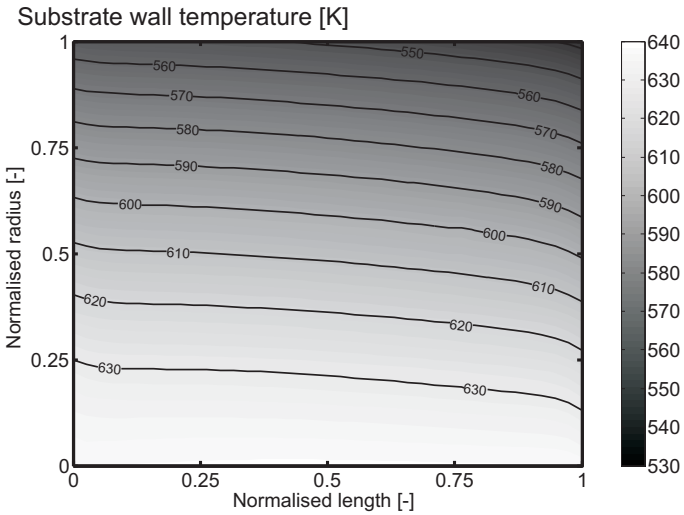

Figure 11: Axisymmetric field of substrate wall temperature with pulsating flow (0.3 bar in amplitude and 66.6 Hz in frequency), $\dot{m}$ = 375 kg/h and T_{in} = 643 K.

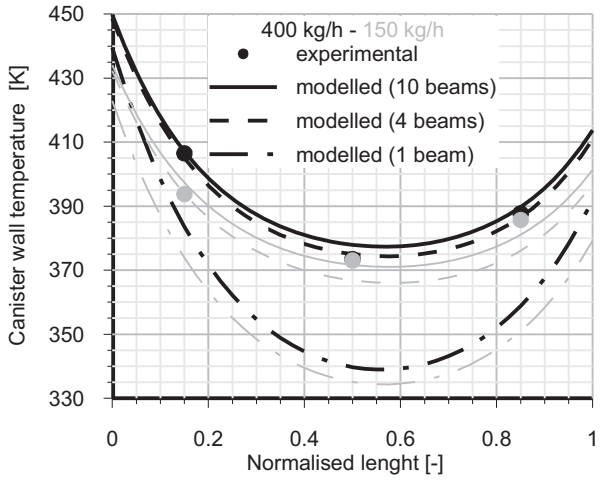

Figure 12: Canister wall temperature prediction. Steady thermal operation with steady flow at T_{in} = 523 K and DPF soot loading equal to 22 g/L.

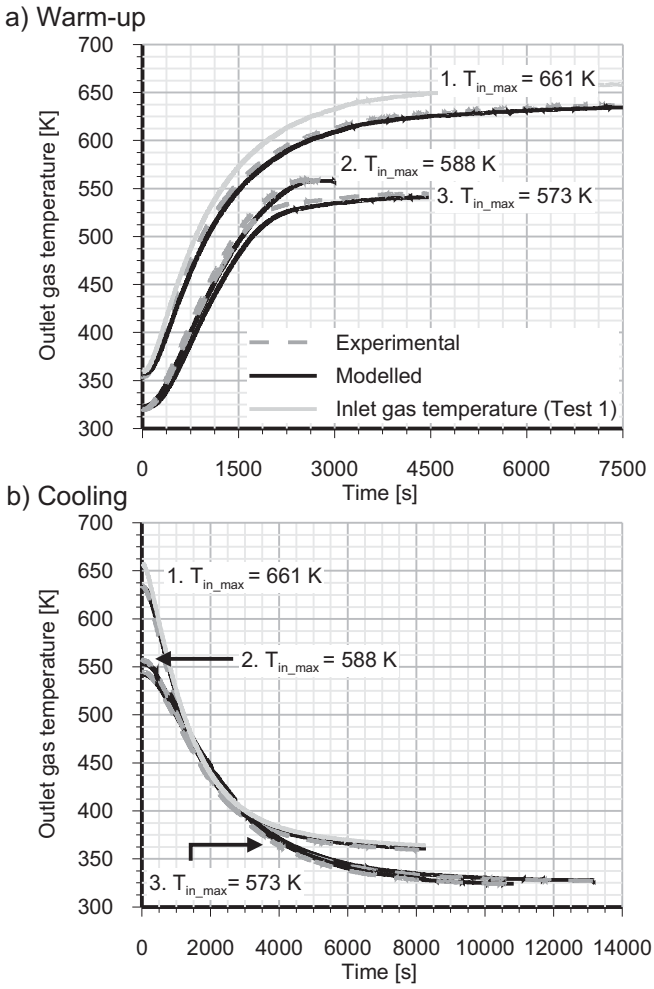

Figure 13: Outlet gas temperature prediction during warm-up and cooling thermal transients up to/from different temperature level. Calculation with 1 channel beam.